

# FRACTURE OF CONCRETE STRUCTURAL MEMBERS SUBJECTED TO BLAST

G. MORALES-ALONSO<sup>\*</sup>, D.A. CENDÓN<sup>†</sup>, F. GÁLVEZ<sup>†</sup> AND V. SÁNCHEZ-GÁLVEZ<sup>†</sup>

<sup>\*</sup>Universidad Politécnica de Madrid (UPM)  
E.T.S.I. Industriales  
c/ José Gutiérrez Abascal, 2. 28006 - Madrid, Spain

<sup>†</sup>Universidad Politécnica de Madrid (UPM)  
E.T.S.I. de Caminos, Canales y Puertos  
c/ Prof. Aranguren s/n. 28040 -Madrid, Spain  
e-mail: dcendon@mater.upm.es

**Key words:** Cohesive fracture, embedded crack, high strain rate, blast loading

**Abstract:** If reinforced concrete structures are to be safe under extreme impulsive loadings such as explosions, a broad understanding of the fracture mechanics of concrete under such events is needed. Most buildings and infrastructures which are likely to be subjected to terrorist attacks are borne by a reinforced concrete (RC) structure. Up to some years ago, the traditional method used to study the ability of RC structures to withstand explosions consisted on a choice between handmade calculations, affordable but inaccurate and unreliable, and full scale experimental tests involving explosions, expensive and not available for many civil institutions. In this context, during the last years numerical simulations have arisen as the most effective method to analyze structures under such events. However, for accurate numerical simulations, reliable constitutive models are needed. Assuming that failure of concrete elements subjected to blast is primarily governed by the tensile behavior, a constitutive model has been built that accounts only for failure under tension while it behaves as elastic without failure under compression. Failure under tension is based on the Cohesive Crack Model. Moreover, the constitutive model has been used to simulate the experimental structural response of reinforced concrete slabs subjected to blast. The results of the numerical simulations with the aforementioned constitutive model show its ability of representing accurately the structural response of the RC elements under study. The simplicity of the model, which does not account for failure under compression, as already mentioned, confirms that the ability of reinforced concrete structures to withstand blast loads is primarily governed by tensile strength.

## 1 INTRODUCTION

Blast and other impulsive or highly dynamic loading of reinforced concrete structures, although being infrequent, have proven to be possible due to different accidental or intentional events. For this reason, the design of buildings and other structures under blast loading has received considerable attention from the community of technicians within the last years.

However, engineers facing the design of reinforced concrete structures able to

withstand explosions have to rely on documents and manuals [1-4] that only provide recommendations and general indications, or rather on their experience and know-how.

From the calculation point of view, the simplest approach is the equivalent static load method [5], in which a static load equivalent to the explosive event is calculated and then applied on the structure as any other loading case.

The advantage of this method is that it is

based on static calculation, which is the most common methodology used by structural engineers. Its main drawback is that it is an excessively simplified approach in which some major factors such as the inertia or the time of response of the structure are not taken into account.

One step forward is the development of single degree-of-freedom systems, as recommended in the TM5-1300 manual from the US Army [3]. The structure is to be modeled as a single dof system of equivalents mass and stiffness. The maximum response of the system can be estimated using elastic-plastic response spectra, see [6-8]. With this approach inertial and strain rate effects can be taken into account. However, the structure is considered to respond global and simultaneously to the blast action and for this reason local failures of structural elements are not accounted for. This is also a major issue, since experience shows that local failure in some structural elements can lead to progressive collapse of the structure, with catastrophic consequences for its occupants [9].

A more realistic and detailed approach to the structural response can be obtained (i) by full scale testing of structures subjected to blast or (ii) through numerical simulation of structures loaded under blast events.

Full scale testing of reinforced concrete structures is expensive and often not available due to lack of permission for explosive handling and for accessing to proper tests fields. Furthermore, the design of structures under blast via trial and error through full scale detonations would require building and detonating as many structures as load cases were considered in the design. Anyway some full scale detonation tests can be found in the scientific literature [10-17].

The numerical simulation approach has been historically limited by the computing power available. However, during the last years this lack of computer power is being overcome and finite element analyses arise as the most suitable and promising method for the design of reinforced concrete structures under impulsive events. However, in order to

get representative numerical results, reliable constitutive models for the materials involved are necessary. There is a broad variety of constitutive models for concrete under high strain rates [18-22] but most of them have never been properly validated through comparison with experimental explosive tests. Moreover, many of them have been developed and validated for their use in the simulation of ballistic penetration events in which the compressive behavior of concrete is of the greater importance. In these models the tensile failure criterion and crack development formulation are often modeled in a rather simple manner, since they play a minor role in penetration events, which seems not to be the case of blast loading [14-17, 23].

In this research a novel constitutive model for concrete subjected to high strain rates is developed. The model has been programmed as a material user subroutine for the LS-DYNA numerical code, and has been validated through comparison with an experimental program previously developed by the authors [23].

The constitutive model is an adaptation of the Strong Discontinuity Approach based model presented in [24, 25] to explicit calculations. It is strain rate sensitive and has been applied to hexaedric single integration point finite elements. These characteristics make it especially suitable for structural concrete elements where dynamic failure is governed by a complex tensile cracking pattern.

## 2 NUMERICAL MODEL

The constitutive model can be briefly described as a model with no failure under compression (behavior linear-elastic in the compressive domain), while failure in tension is modeled through the Cohesive Crack Model once a threshold value for the maximum principal stress is exceeded. The cohesive crack is inserted in the finite elements through the Embedded Crack Approach (or Strong Discontinuity Approach).

## 2.1 The Cohesive Crack Model

Concrete is a quasi-brittle material that can be roughly considered as linear elastic under mode I (pure tension) loading until it reaches its tensile strength. When the tensile strength is exceeded, damage appears in the material and the stresses that it can withstand are progressively reduced. According to the Cohesive Crack Model, or Fictitious Crack Model [26] damage is assumed to concentrate in a discontinuity line, and it is governed by a relationship between the crack opening,  $w$ , and the mode I stress transmitted across the crack sides through a certain mathematical function  $f(w)$ , called *softening curve* (figure 1). An extensive review of this model can be found in [27].

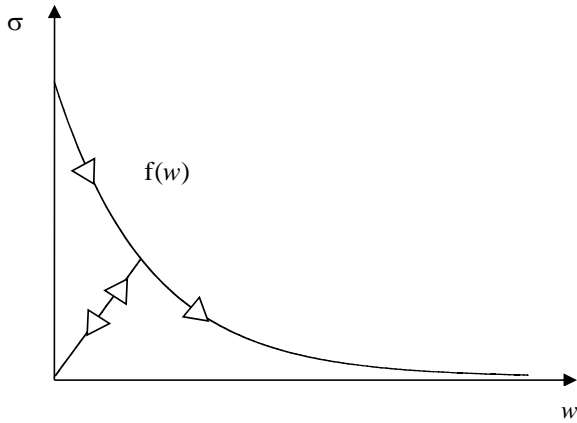


Figure 1: Softening curve.

To generalize to 3D mixed mode crack opening the abovementioned mode I behavior, a central force model has been used as in [24]. According to this central forces model, it is assumed that the traction vector  $\mathbf{t}$  between crack borders is parallel to the crack displacement vector  $\mathbf{w}$ , see figure 2. Therefore, the expression of the traction vector reads:

$$\mathbf{t} = \frac{f(\tilde{w})}{\tilde{w}} \cdot \mathbf{w} \quad (1)$$

Being  $\tilde{w} = \max(|\mathbf{w}|)$  an equivalent crack opening value defined as the maximum registered opening in the crack and  $f(\tilde{w})$  the softening function that relates the stress across the crack with crack opening.

In the absence of specific tests to determine the precise shape of the softening curve, the exponential one [27] has been chosen for the simulations presented here, although linear and bilinear approximations have been also implemented in the model. The exponential approach is thought to be a good option for both its simplicity and the continuity of its derivatives. According to expression (1), unloading-reloading is assumed to follow a linear path, as shown in figure 1.

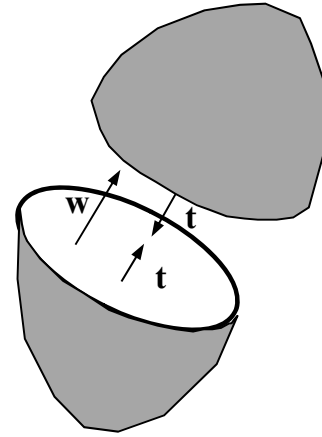


Figure 2: Central forces model.

## 2.2 The embedded crack approach

Equation (1) provides the traction vector  $\mathbf{t}$  acting between both sides of the crack. However, in order to apply such traction, a crack must be first inserted somehow in the mesh. Such issue has been addressed by means of the embedded crack approach [24, 25, 28-30].

The kinematics describing a strong discontinuity, such as a crack, embedded on finite elements can be obtained by decoupling the displacement field into a continuous and a discontinuous part. In this decoupling the discontinuous part lumps the additional degrees of freedom related with the discontinuity, namely opening and sliding, which are incorporated through the displacement jump vector,  $\mathbf{w}$ .

Let us consider a quite general finite element like the one depicted in figure 3. The element is crossed by a crack which divides it into the  $A^-$  and  $A^+$  regions, as shown in the

figure. The crack orientation is defined by the  $\mathbf{n}$  vector, which is the unitary vector normal to the crack line. The jump in displacements is given by the  $\mathbf{w}$  vector, which will be enforced to have a constant value along the crack embedded in the element. According to [31] the equation that describes the displacement field in the element under these conditions is given by:

$$\mathbf{u}(\mathbf{x}) = \sum_{\alpha \in A} N_{\alpha}(\mathbf{x}) \cdot \mathbf{u}_{\alpha} + \left[ H(\mathbf{x}) - \sum_{\alpha \in A^+} N_{\alpha}(\mathbf{x}) \right] \cdot \mathbf{w} \quad (3)$$

Where  $\alpha$  is the node index,  $N_{\alpha}(\mathbf{x})$  is the shape function associated to node  $\alpha$ ,  $\mathbf{u}_{\alpha}$  is the corresponding nodal displacement vector,  $\mathbf{w}$  is the displacement jump vector and  $H(\mathbf{x})$  is the Heaviside function ( $H(\mathbf{x}) = 0$  if  $\mathbf{x} \in A^-$ ;  $H(\mathbf{x}) = 1$  if  $\mathbf{x} \in A^+$ ).

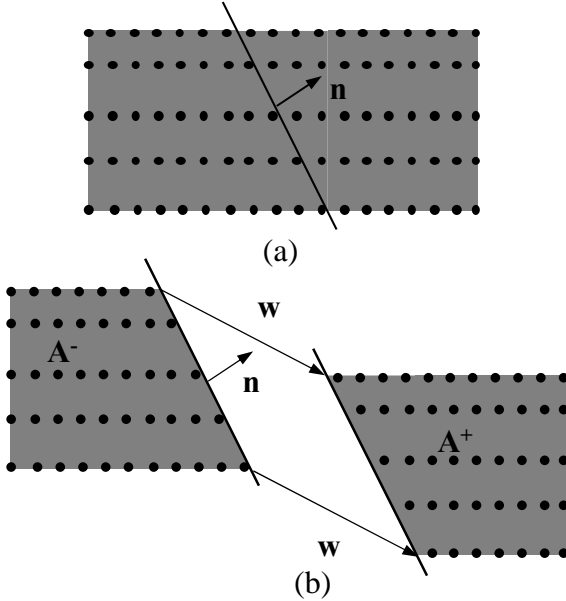


**Figure 3:** Arbitrary finite element with (a) discontinuity line and (b) displacement jump through the discontinuity line.

The strain tensor can be obtained from the displacement field by taking the symmetric gradient to eqn. (3), leading to:

$$\boldsymbol{\varepsilon}^c(\mathbf{x}) = \sum_{\alpha \in A} [\mathbf{b}_{\alpha}(\mathbf{x}) \otimes \mathbf{u}_{\alpha}]^s - \left[ \left( \sum_{\alpha \in A^+} \mathbf{b}_{\alpha}(\mathbf{x}) \right) \otimes \mathbf{w} \right]^s \quad (4)$$

, where  $\mathbf{b}_{\alpha}(\mathbf{x}) = \mathbf{grad} N_{\alpha}(\mathbf{x})$ . In eqn. (4) the first term represents the strain field that would

have the element if no displacement discontinuity were present on it, given that for this term the strain field is obtained from taking the derivative to the shape functions directly applied to the nodal displacements. For that reason, from now on we will name:

$$\boldsymbol{\varepsilon}^a(\mathbf{x}) = \sum_{\alpha \in A} [\mathbf{b}_{\alpha}(\mathbf{x}) \otimes \mathbf{u}_{\alpha}]^s \quad (5)$$

, in which the superscript  $a$  stands for *apparent*. The second term in eqn. (4) represents the amount that must be subtracted to the apparent strains in order to take into account for the presence of the crack. For the sake of simplicity, we will adopt the following notation:

$$\mathbf{b}^+(\mathbf{x}) = \sum_{\alpha \in A^+} \mathbf{b}_{\alpha}(\mathbf{x}) \quad (6)$$

Therefore, the  $\mathbf{b}^+$  vector is obtained as the sum of the gradients of the shape functions corresponding to the nodes belonging to the  $A^+$  region. From now on, these nodes will be referred to as *solitary nodes*. Consequently, the choice of the solitary nodes becomes a key issue in the formulation of the embedded crack model, since they determine the kinematics of the model. By substituting eqns. (5) and (6) in (4), we obtain:

$$\boldsymbol{\varepsilon}^c(\mathbf{x}) = \boldsymbol{\varepsilon}^a(\mathbf{x}) - [\mathbf{b}^+(\mathbf{x}) \otimes \mathbf{w}]^s \quad (7)$$

### 2.3 Initiation and orientation of the crack

Maximum principal stress is used to obtain both the crack initiation and the crack orientation. Once the maximum principal stress overcomes the tensile strength, a crack is introduced perpendicular to the direction of the former. Therefore the crack orientation  $\mathbf{n}$  is computed as the unit eigenvector associated to such maximum principal stress. In principle, for a given element, there should be as many principal stress directions as integration points were present in the element. This issue is circumvented by applying this methodology only to constant stress elements, as made earlier by [24, 25, 28-30]. For the model

developed here, 3D hexahedral single integration point elements have been used.

However, by setting the crack direction the problem of deciding which are the solitary nodes is not solved. Figure 4 shows some of the possible solitary nodes combinations for a given crack direction associated to a certain  $\mathbf{n}$  vector.

Among all the possible combinations of solitary nodes and, subsequently of possible  $\mathbf{b}^+$  vectors, in this work similarly to [24, 32] the solitary nodes are determined by requiring that the angle between vectors  $\mathbf{n}$  and  $\mathbf{b}^+$  is the smallest possible:

$$\frac{\mathbf{n} \cdot \mathbf{b}^+}{|\mathbf{b}^+|} = \max \quad (8)$$

All this procedure of calculating  $\mathbf{n}$  and  $\mathbf{b}^+$  takes place locally every time a finite element exceeds the maximum principal stress criterion and no crack continuity is enforced between adjacent elements. At first stages of the crack development, stress waves in the material may cause an element to crack on a different direction of the adjacent element pre-existing crack, thus producing an undesirable crack locking effect. To avoid this problem without introducing crack continuity algorithms, the concept of crack adaptation, firstly introduced by [24], is adopted here.

This approach allows the crack to adapt itself to later variations of its principal stress direction while its opening does not overcome a certain threshold value. Once such value is exceeded, the crack direction is frozen. For the simulations presented here, the value of  $w_{adapt}=0.1G_F/f_t$  has been chosen, being  $w_{adapt}$  the threshold crack opening value,  $G_F$  the specific fracture energy, and  $f_t$  the tensile strength.

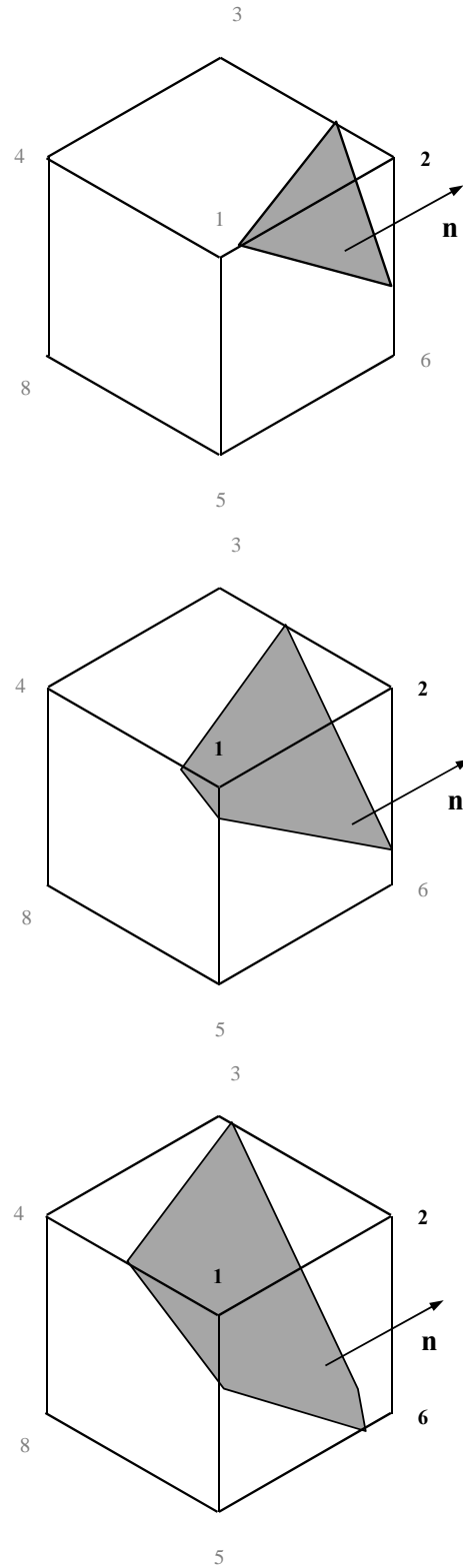


**Figure 4:** Examples of some of the different solitary nodes combinations for a unique crack orientation when varying its position, where the solitary nodes are printed in bold letters.

The use of hexahedral elements instead of tetrahedrons offers two major advantages. First of all, the whole element presents more possible combinations of solitary nodes and, subsequently, more possible  $\mathbf{b}^+$  vectors to find the more parallel one to the  $\mathbf{n}$  direction, following eqn. (8). This fact provides an element kinematics more compliant with the crack orientation, according to the maximum principal stress criterion.

The second advantage appears when a structured mesh is used. Since the  $\mathbf{b}^+$  vector is obtained as the gradient of the shape functions corresponding to the solitary nodes, global coordinates of these nodes would be required to obtain such vector. Many commercial explicit codes, such as LS-DYNA or AUTODYN, do not allow user programmed elements and only material user subroutines are available. Unfortunately, nodal coordinates are not usually accessible at the material level (integration point level). However in case of using a structured mesh of hexahedral elements, for all the elements present in the mesh the eight shape functions of all elements are equal eight to eight with the only difference of being translated in the XYZ space. Since the  $\mathbf{b}^+$  vector comes from the gradient of the shape functions and the spatial translation does not affect the result of the gradient, all the possible  $\mathbf{b}^+$  vectors for all elements are exactly the same. Then, the only required parameters are the lengths of the hexahedra sides, which can be input to the subroutine as any other material property. This strategy makes possible the use of this material model in a wide variety of commercial and non commercial numerical codes. The only price to pay is that nodal positions cannot be obviously updated and therefore it is only suitable for small displacement analyses.

## 2.4 Local equilibrium

As it has been aforementioned, the material behaves as linear elastic until the maximum principal stress exceeds the threshold value of the tensile strength. At this moment the cohesive crack is embedded in the element. Since outside the crack the material continues

behaving linear elastic, we can obtain the stress tensor by applying:

$$\boldsymbol{\sigma} = \mathbf{D} \cdot \boldsymbol{\varepsilon}^c \quad (9)$$

, being  $\mathbf{D}$  the elastic moduli fourth order tensor. By substituting  $\boldsymbol{\varepsilon}^c$  by its value according to eqn. (7), now it reads:

$$\boldsymbol{\sigma} = \mathbf{D} \cdot [\boldsymbol{\varepsilon}^a - \mathbf{b}^+ \otimes \mathbf{w}]^s \quad (10)$$

The previous expression provides Cauchy's stress tensor in the continuum part of the element. However the traction vector acting along the crack sides must satisfy local equilibrium with the abovementioned stress tensor. In other words, the traction vector corresponding to the  $\mathbf{n}$  direction applied to Cauchy's tensor of the continuum must be equal to the crack's traction vector:

$$\mathbf{t}_{\text{crack}} = \frac{f(\tilde{w})}{\tilde{w}} \cdot \mathbf{w} \quad (11)$$

$$\mathbf{t}_{\text{continuum}} = (\mathbf{D} \cdot \boldsymbol{\varepsilon}^c) \cdot \mathbf{n} = [\mathbf{D} \cdot \boldsymbol{\varepsilon}^a - \mathbf{D} \cdot [\mathbf{b}^+ \otimes \mathbf{w}]^s] \cdot \mathbf{n} \quad (12)$$

$$\begin{aligned} \mathbf{t}_{\text{crack}} &= \mathbf{t}_{\text{continuum}} \rightarrow \\ \rightarrow \frac{f(\tilde{w})}{\tilde{w}} \cdot \mathbf{w} &= \mathbf{D} \cdot [\boldsymbol{\varepsilon}^a - [\mathbf{b}^+ \otimes \mathbf{w}]^s] \cdot \mathbf{n} \quad (13) \end{aligned}$$

Equation (13) is the basic equation governing the cohesive embedded crack formulation. In the equation, the only unknown is the crack displacements vector,  $\mathbf{w}$ , and must be solved by numerical methods.

## 2.5 Rate effects

In a reinforced concrete element subjected to a blast event, the load is applied at a very high strain rate, within the order of  $10 \text{ s}^{-1}$  to  $1000 \text{ s}^{-1}$  [33, 34]. While the mechanical properties of almost all materials are strain rate sensitive, the effect of high strain rates is particularly remarkable in the case of concrete.

The most usual way of taking into account the effect of strain rates is through the *Dynamic Increase Factor* (DIF), which is obtained as the ratio between the dynamic and the static strength. The DIF is normally

defined for the compressive strength and the tensile strength [34-36].

Some attempts have been also made to obtain the DIF for the fracture energy of concrete [37-39]. Although the experimental data are scarce, it seems that the DIF for fracture energy is very similar to the DIF for the tensile strength. Therefore, in this research a multiplicative formulation has been used to take into account for rate effects. It consists on multiplying the whole softening curve by the DIF, as shown in figure 5. As a result, both the tensile strength and the fracture energy are simultaneously increased by the same factor, in line with the experimental results obtained by [38]. The expression of the DIF applied in this research is the one provided for the tensile strength by the CEB Bulletin 187 [35]:

$$DIF = \frac{f_{td}}{f_{ts}} = \left[ \frac{\dot{\varepsilon}}{\dot{\varepsilon}_0} \right]^{1.016\alpha} \quad \text{for} \quad \varepsilon \leq 30 \text{ s}^{-1} \quad (16)$$

$$DIF = \frac{f_{td}}{f_{ts}} = \eta \cdot \dot{\varepsilon}^{\frac{1}{3}} \quad \text{for} \quad \varepsilon > 30 \text{ s}^{-1}$$

Where  $\delta = \frac{1}{10 + \frac{1}{2} \cdot f_{ts}}$  and  $\eta = 10^{6.933\delta - 0.492}$ ,

$f_{td}$  and  $f_{ts}$  are the dynamic and static tensile strengths of concrete, respectively,  $f_{cs}$  is the static compressive strength of concrete,  $f_{c0}$  is a reference value equal to 10 MPa,  $\varepsilon$  is the actual strain rate and  $\varepsilon_s$  is the static strain rate, which is taken as  $10^{-6} \text{ s}^{-1}$ .

### 3 EXPERIMENTAL RESULTS

The experimental program developed by the authors used to validate the model consisted of open air detonations over reinforced concrete square slabs simply supported on their four corners. Two different grades of concrete were tested: normal strength concrete (NSC) and high strength concrete (HSC). With each detonation, the test setup allowed to test three slabs

simultaneously, placed at 1.50 m from the explosive charge. Two detonations of 5 kg TNT equivalent were performed for each concrete grade, which represents a total of 6 plates of each kind concrete, all them subjected to the same explosive load. The geometry of the plates is provided in figure 6. Compressive strength of both concretes, measured according to the EHE 08 Spanish concrete structural code [40] at the age of the tests is given in table 1.

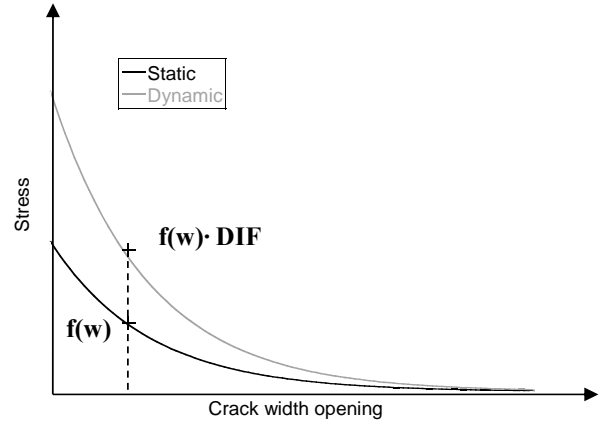


**Figure 5:** Exponential softening function original and enhanced due to strain rate.

**Table 1:** Evolution of concrete strength

Age [days]	NSC $f_{ck}$ [MPa]	NSC $f_{ck}$ [MPa]
28	49.81	91.07

As shown in figure 6, slabs were reinforced on their back side with a steel mesh of bars of 6 mm diameter of steel grade B 500 S, spaced 150 mm in both directions. For further details about the experimental campaign, the reader is addressed to [23].

The test setup did not allow measuring neither loads nor displacements, and its main purpose was to study the differences on failure and crack patterns between both kinds of concretes given that they were subjected to the same explosive charge.

Although the slabs showed experimental scattering on their cracking pattern and damage level, two different modes of cracks were clearly observed after the tests: a shear failure mode, depicted by the circular-like

cracks surrounding the supports, and a bending failure mode represented by cracks parallel to the sides of the slabs. These crack modes are shown in figure 7.

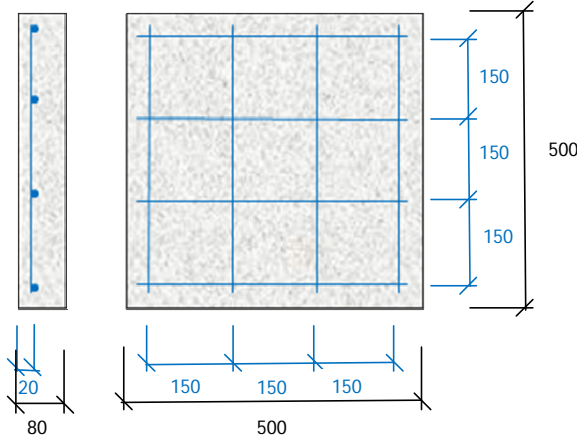


**Figure 6:** Test specimen geometry and reinforcement details (dimensions in mm).

When comparing the behavior of the two different grades of concrete, it was noted that although in principle all slabs failed with multiple cracks going through their thickness, the dominant cracking mode in the case of normal strength concrete was the shear one, while in the case of the high strength concrete bending mode cracks were more remarkable.

From a simple theoretical analysis based on the yield line method, a slab supported on its four corners and subjected to a uniformly distributed static load should fail under pure-bending mode. However, the experimental results obtained in the abovementioned campaign demonstrate that the loading rate can change the failure mode of a structural concrete element. Moreover, the change in the failure mode is not only dependent on the loading rate, but also on the concrete quality. Similar results were obtained on an experimental campaign performed on reinforced concrete beams by [14-15].

## 4 NUMERICAL SIMULATION

### 4.1 Model setup

The experimental campaign summarized in the previous section was simulated by using

the model presented in this paper. LS-DYNA v.761 explicit finite element code was used for such task. Since constant stress hexahedral elements were used, it was possible to implement the constitutive model at a material level, therefore a user subroutine was enough to implement it.

Concrete plates were meshed with 4x4x4mm one point integration solid (brick) elements, resulting in a total of 546000 elements.

Steel rebar was modeled through 1500 truss elements of 4mm length. Bond between concrete and rebar was set through using common nodes on steel and concrete meshes, which is equivalent to assume perfect bonding between concrete and rebar.

The material parameters input for the concrete model are given in table 2.

Steel rebar was modeled using a elastic-plastic material model, with the parameters given in table 3.

**Table 2:** Mechanical properties for concrete

	NSC	HSC
Density [kg/m <sup>3</sup> ]	2400	2400
Elasticity modulus [MPa]	38600	46200
Poisson's ratio [-]	0.2	0.2
Static tensile strength* [MPa]	4.1	6.1
Static fracture energy* [N/m]	123.4	187.7
Static compressive strength** [MPa]	49.8	91.0

\* Values estimated according to the CEB-FIP Model Code [4]

\*\*Compressive strength is only necessary to take into account rate effects, according to eqn. (16).

**Table 3:** Mechanical properties for steel

Density [kg/m <sup>3</sup> ]	7850
Elasticity modulus [MPa]	205000
Yield stress [MPa]	500.0
Poisson's ratio [-]	0.30

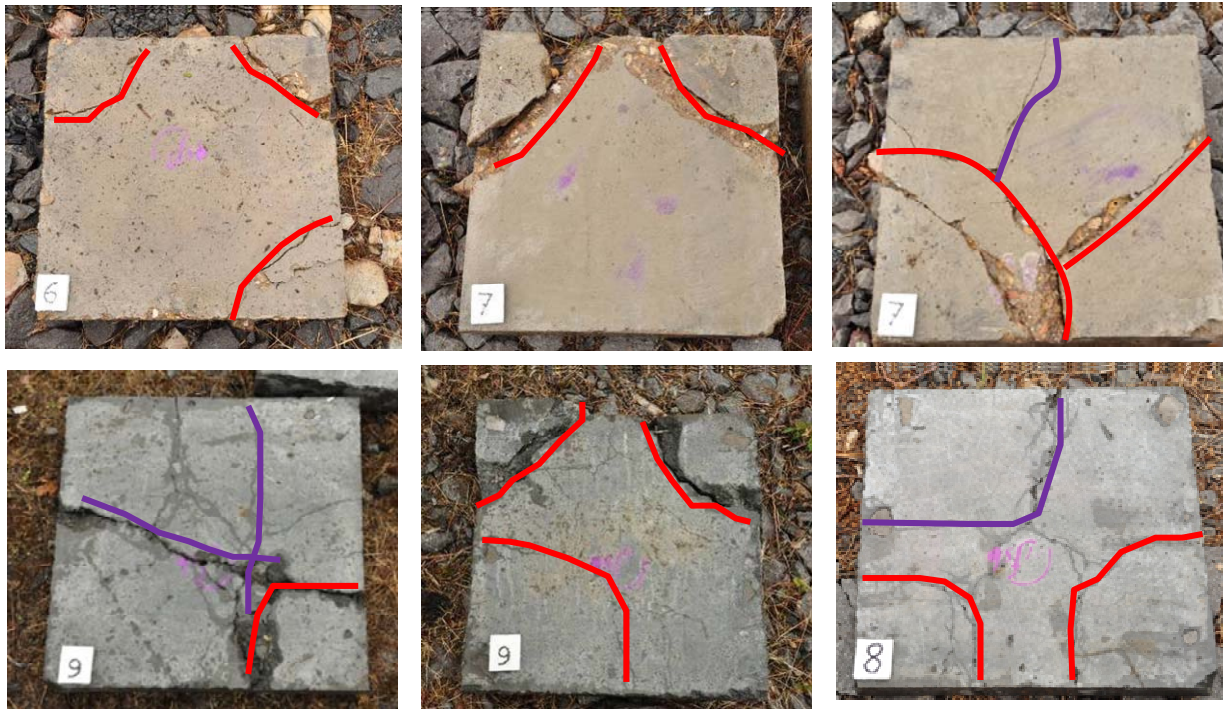


**Figure 7:** Slabs after detonation tests with highlighted cracks (bending cracks in purple, shear cracks on red).

Loading of slabs was imposed by applying directly the reflected pressure–time history that was measured by piezoelectric pressure gauges during the tests [23].

In order to get a better representation of the crack patterns in the simulations, the *crack visibility* parameter has been defined. The minimum visible crack is around 0.1 and 0.2 mm, therefore crack openings below this threshold would not be visible by naked eye. Then, we have defined *crack visibility* as the integer part of the division of the norm of the crack opening vector,  $|\mathbf{w}|$ , over the minimum visible crack width (0.15 mm has been used in these simulations). Therefore, a crack opening below the minimum visible crack threshold would result in a *crack visibility* value of 0, while for example a crack opening of 0.48 would result in a value of 3 in this case.

Figure 9 shows the crack visibility patterns obtained after 5ms of simulation, when the loading process has been finished and the plates have been fully unloaded. It can be observed how the model succeeds in catching the different failure patterns between both concretes.

The reason for such different cracking patterns between both concrete grades appears

to be that crack initiation takes place at the first moments of stress wave propagation within the concrete. The shock wave impact on the slab generates tensile stress waves in the material that travel from the supports to the center of the slab. These tensile stress waves are of the same magnitude in both concrete types, but the ability to withstand them is greater in HSC, due to its greater tensile strength. For this reason, as tensile strength of NSC does not suffice to withstand the tensile stress waves, the material fails near the supports. Nevertheless, on HSC these waves also cause failure of the concrete near the supports, but on a much smaller extent. Therefore, the stress waves can propagate further on the HSC slabs, reaching the center span of the slab, where they cause a greater damage.

Later on the inertial effects on both NSC and HSC slabs make the cracks develop, being the increase of width opening greater on the cracks where the original damage was originally bigger, that is, near the supports on NSC slabs and on center span on HSC slabs.

As in the experimental campaign, numerical simulations also show how in the two kinds of concrete grades both shear and bending cracks

are however present but always one type of crack is dominant, making the other one difficult to be seen by naked eye.

The numerical simulations have also been able to represent the fact that after the tests the shear cracks on NSC slabs showed a greater width than the ones in HSC, see figure 8.

## 5 CONCLUSIONS

A new material model for concrete subjected to blast and explosions has been developed. The model is based on the embedded crack approach in conjunction with the cohesive crack concept. Strain rate effects are taken into account following a multiplicative approach by using the *Dynamic Increase Factor* (DIF) applied to the tensile strength and subsequently to fracture energy.

The model has been developed for constant stress hexahedral elements. This has made possible to program it at a material level, avoiding the need of enquiring the nodal coordinates for the  $\mathbf{b}^+$  vector calculation, making easier to implement it in a commercial finite element explicit code, such as LS-DYNA.

An experimental campaign previously developed by the authors on reinforced concrete slabs of two different concrete grades has been used to validate the model. The numerical simulations have shown its capability on reproducing the predominant crack paths and failure patterns with good accuracy level.

Numerical simulations, besides experimental results, show how both, the high strain rates and the concrete tensile strength, influence the crack patterns and the failure modes of concrete structural elements. This issue is remarkably important, since shear failure usually lead to less ductile behavior and must be avoided as much as possible by structural engineers.

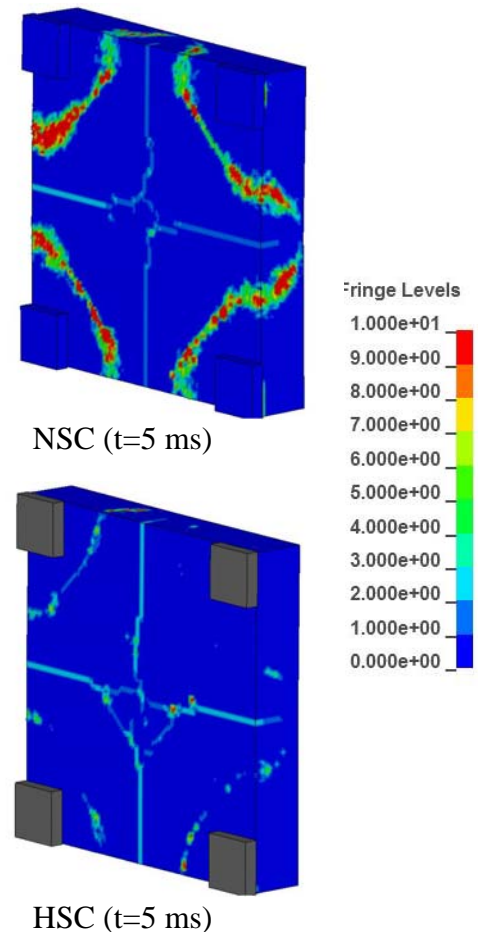


Figure 8: Crack visibility contours.

## ACKNOWLEDGEMENTS

The authors would like to acknowledge the Spanish Ministries Ministerio de Fomento and Ministerio de Ciencia e Innovación, by founding this research through program P16/08 (NCEX), also to the Fundación Agustín de Betancourt for the economical support provided and to the Fundación Santa Bárbara for their help with the experimental program.

## REFERENCES

- [1] U.S. Department of the Army, Navy and Air Force, 1986. Fundamentals of Protective Design for Conventional Weapons, TM 5-855-1.
- [2] Air Force Engineering and Services Center, 1989. Protective Construction Design Manual. ESL-TR-87-57. Engineering and Services Laboratory, Tyndall Air Force Base, Florida.

- [3] U.S. Department of the Army, 1990. Design of structures to resist the effects of accidental explosions. US Department of the Army Technical Manual, TM5-1300, Washington DC.
- [4] Comité Euro-International du Béton, 2012. Model Code 2010. Lausanne, FIB.
- [5] Anwarul Islam, A.K.M., Yazdani, N., 2008. Performance of AASHTO girder bridges under blast loading. *Eng. Structures*, vol 30, p. 1922-1937.
- [6] Gantes, C.J., Pnevmatikos, N.G., 2004. Elastic-plastic response spectra for exponential blast loading. *Int. J. of Impact Eng.*, vol. 30, p. 323-343.
- [7] Yang, G., Lok, T.-S., 2007. Analysis of RC structures subjected to air-blast loading accounting for strain rate effect of steel reinforcement. *Int. J. of Impact Eng.*, vol. 34, p. 1924-1935.
- [8] Fischer, K., Häring, I., 2009. SDOF response model parameters from dynamic blast loading experiments. *Eng. Structures*, vol. 31, n° 8, p. 1677-1686.
- [9] Dusenberry, D.O., 2010. Handbook for Blast Resistant Design of Buildings. John-Wiley & Sons.
- [10] Zhou, X.Q., Kuznetsov, V. A., Hao, H., Waschl, J., 2008. Numerical prediction of slab response to blast loading. *Int. J. of Impact Eng.*, vol. 35, p. 1186-1200.
- [11] Luccioni, B., Luege, M., 2006. Concrete pavement slab under blast loads. *Int. J. of Impact Eng.*, vol. 32, p. 1248-1266.
- [12] Mays, G.C., Hetherington, J.G., Rose, T.A., 1999. Response to blast loading of concrete wall panels with openings. *ASCE J. Struct. Eng.*, vol. 125.
- [13] Ellis, B.R., Tsui, F., 1997. Testing and analysis of reinforced concrete panels subject to explosive and static loading. *Proc Instn Civ Eng.*
- [14] Magnusson, J., Hallgren, M., Ansell, A., 2010. Air-blast-loaded, high-strength concrete beams. Part I: Experimental investigation. *Mag. Concrete Research*, vol. 62, No. 2, p. 127-136.
- [15] Magnusson, J., Ansell, A., Hansson, H., 2010. Air-blast-loaded, high-strength concrete beams. Part II: Numerical non-linear analysis. *Mag. Concrete Research*, vol. 62, No. 4, p. 235-242.
- [16] Schenker, A., Anteby, I., Gal, E., Kivity, Y., Nizri, E., Sadot, O., Michaelis, R., Levintant, O., Ben-Dor, G., 2008. Full-scale field tests of concrete slabs subjected to blast loads. *Int. J. of Impact Eng.*, vol. 35, p. 184-198.
- [17] Razaqpur, A.G., Tolba, A., Contestabile, E., 2007. Blast loading response of reinforced concrete panels reinforced with externally bonded GFRP laminates. *Composites: Part B*, vol. 38, p. 535-546.
- [18] Malvar, L.J., Crawford, J.E., Wesevich, J.W., Simons, S.D., 1997. A plasticity concrete material model for DYNA3D. *Int. J. of Impact Eng.*, vol. 19, p. 847-873.
- [19] Broadhouse, B.J., 1995. The Winfrith concrete model in LS-DYNA3D. Report: SPD/D(95)363, Structural Performance Department, AEA Technology, Winfrith Technology Centre, U.K.
- [20] Holmquist, T.J., Johnson, G.R., Cook, W.H., 1993. A computational constitutive model for concrete subjected to large strains, high strain rates and high pressures. *Proc. of 14th International Symposium on Ballistics*.
- [21] Gebbeken, N., Ruppert, M., 2000. A new material model for concrete in high-dynamic hydrocode simulations. *Arch. Appl. Mech.*, vol. 70, p. 463-478.
- [22] Cullis, I.G., Schofield, J., Whitby, A., 2010. Assessment of blast loading effects - Types of explosion and loading effects. *Int. J. of Pressure Vessels and Piping*, vol. 87, p. 493-503.
- [23] Morales-Alonso, G., Cendón, D.A., Gálvez, F., Erice, B., Sánchez-Gálvez, V., 2011. Blast Response Analysis of Reinforced Concrete Slabs: Experimental Procedure and Numerical Simulation. *J. of App. Mech.* 78:051010-1-051010-12.
- [24] Sancho, J.M., Planas, J., Cendón, D.A., Reyes, E., Gálvez, J.C., 2007. An embedded crack model for finite element analysis of concrete fracture. *Eng. Fracture Mech.*, vol. 74, pp. 75-86
- [25] Sancho, J.M., Planas, J., Fathy, A.M., Gálvez, J.C., Cendón, D.A., 2007. Three-

- dimensional simulation of concrete fracture using embedded crack elements without enforcing crack path continuity. *Int. J. Numer. Anal. Meth. Geomech.*, vol. 31, pp. 173-187.
- [26] Hillerborg, A., Modeer, M., Petersson, P., 1976. Analysis of crack formation and crack growth in concrete by means of fracture mechanics and finite elements. *Cem. and Concr. Res.* 6: 773-82.
- [27] Bazant, Z.P., Planas, J., 1998. Fracture and size effect in concrete and other quasibrittle materials. CRC Press.
- [28] Jirásek M., 2000. Comparative study on finite elements with embedded cracks. *Comp. Meth. in App. Mech. and Eng.* 188: 307-330.
- [29] Alfaiate, J., Wells, G.N., Sluys, L.J., 2002. On the use of embedded discontinuity elements with crack path continuity for mode-I and mixed-mode fracture. *Eng. Fracture Mech.*, vol. 69, pp. 661-686
- [30] Feist, C., Hofstetter, G., 2006. An embedded strong discontinuity model for cracking of plain concrete. *Computer Methods in Applied Mech. and Eng.*, vol. 195, pp. 7115-7138
- [31] Oliver, J., 1996. Modelling strong discontinuities in solid mechanics via strain softening constitutive equations. Part I: fundamentals. Part 2: numerical simulation. *Int. J. for Numerical Methods in Engineering*, 39, 3575-3623.
- [32] Borja, R.I., 2000. A finite element model for strain localization analysis of strongly discontinuous fields based on standard Galerkin approximation. *Comp. Meth. in App. Mech. and Eng.* 190:1529-1249.
- [33] Bischoff, P.H., Perry, S.H., 1991. Compressive behavior of concrete at high strain rates. *Materials and Structures*, vol. 24, n° 6, p. 425-450.
- [34] Malvar, L.J., Crawford, J.E., 1998. Dynamic increase factors for concrete. *28th DDESB Seminar*.
- [35] Comité Euro-International du Béton, 1988. Bulletin d'Information 187. Concrete structures under impact and impulsive loading. Dubrovnik.
- [36] Ross, C.A., Tedesco, J.W., Kuennen, S.T., 1995. Effects of Strain Rate on Concrete Strength. *ACI Materials Journal*, Vol. 92, No. 1, pp. 37-47.
- [37] Schuler, H., Mayrhofer, C., Thoma, K., 2006. Spall experiments for the measurement of the tensile strength and fracture energy of concrete at high strain rates. *Int. J. of Impact Eng.*, vol. 32, pp. 1635-1650.
- [38] Weerheijm, J., Van Doormaal, J.C.A.M., 2007. Tensile failure of concrete at high loading rates: New test data on strength and fracture energy from instrumented spalling tests. *Int. J. of Impact Eng.*, vol. 34, pp. 609-626.
- [39] Zhang, X.X., Ruiz, G., Yu, R.C. and Tarifa, M., 2009. Fracture behaviour of high strength concrete at a wide range of loading rates. *Int. J. of Impact Eng.*, vol. 36, pp. 1204-1209.
- [40] Comisión Permanente del Hormigón. EHE-08. Instrucción de Hormigón Estructural. R.D. 1247/2008.